

Impact of composition ratio on the structure and optical properties of (1-□)MnFe2O4/(□)ZnMn2O4 nanocomposite

Zein K. Heiba1, Mohamed Bakr Mohamed1,2,†, Ali A. Alkathiri3, Sameh I. Ahmed3, A A Alhazime2
Citation: Chin. Phys. B, 2022, 31 (7): 077102 DOI: 10.1088/1674-1056/ /ac600f
Journal homepage: http://cpb.iphy.ac.cn; http://iopscience.iop.org/cpb

What follows is a list of articles you may be interested in

Spin freezing in the van der Waals material $Mn_2Ga_2S_5$

Jie Shen(沈洁), Xitong Xu(许锡童), Miao He(何苗), Yonglai Liu(刘永来), Yuyan Han(韩玉岩), and Zhe Qu(屈哲)
Chin. Phys. B, 2022, 31 (**6**): 067105. DOI: 10.1088/1674-1056/ac657c

Interfacial defect engineering and photocatalysis properties of hBN/MX_2 (M = Mo, W, and X = S, Se heterostructures

Zhi-Hai Sun(孙志海), Jia-Xi Liu(刘佳溪), Ying Zhang(张颖), Zi-Yuan Li(李子源), Le-Yu Peng(彭乐宇), Peng-Ru Huang(黄鹏儒), Yong-Jin Zou(邹勇进), Fen Xu(徐芬), and Li-Xian Sun(孙立贤)
Chin. Phys. B, 2022, 31 (**6**): 067101. DOI: 10.1088/1674-1056/ac43b2

Evolution of optical properties and molecular structure of PCBM films under proton irradiation

Guo-Dong Xiong(熊国栋), Hui-Ping Zhu(朱慧平), Lei Wang(王磊), Bo Li(李博), Fa-Zhan Zhao(赵发展), and Zheng-Sheng Han(韩郑生)
Chin. Phys. B, 2022, 31 (**5**): 057102. DOI: 10.1088/1674-1056/ac322b

First-principles calculations of the hole-induced depassivation of SiO_2/Si interface defects

Zhuo-Cheng Hong(洪卓呈), Pei Yao(姚佩), Yang Liu(刘杨), and Xu Zuo(左旭)
Chin. Phys. B, 2022, 31 (**5**): 057101. DOI: 10.1088/1674-1056/ac3506

Topological properties of Sb(111) surface: A first-principles study

Shuangxi Wang(王双喜) and Ping Zhang(张平)
Chin. Phys. B, 2022, 31 (**4**): 047105. DOI: 10.1088/1674-1056/ac46bc

---

Impact of composition ratio on the structure and optical properties of $(1-x)MnFe_2O_4/(x)ZnMn_2O_4$ nanocomposite

Zein K. Heiba[1], Mohamed Bakr Mohamed[1,2,†], Ali A. Alkathiri[3], Sameh I. Ahmed[3], A A Alhazime[2]

[1] *Department of Physics, Faculty of Science, Ain shams University, Cairo* 11566, *Egypt*
[2] *Physics Department, Faculty of Science, Taibah University, Al-Madina al Munawarah, Saudi Arabia*
[3] *Depatment of Physics, College of Science, Taif University, P. O. Box* 11099, *Taif* 21944, *Saudi Arabia*

(Received 12 December 2021; revised manuscript received 13 March 2022; accepted manuscript online 23 March 2022)

$(1-x)MnFe_2O_4$ (MFO)/$xZnMn_2O_4$ (ZMO) ($x = 0$, 0.2, 0.5, 0.8, and 1.0) nanocomposite samples were prepared using co-precipitation procedure. The phase percentage, cell parameters, and crystallite size of MFO and ZMO phases in each nanocomposite sample were calculated using Rietveld refinement procedure. The x-ray diffraction (XRD) analysis and Fourier-transform infrared spectroscopy techniques established the variation in the lattice parameters of each phase are due to permutation of all cations among the octahedral and tetrahedral sites of MFO and ZMO. The different oxidation states of different ions in all samples were determined using x-ray photoelectron spectroscopy (XPS) technique. The variation in absorbance of the nanocomposite samples with composition parameter (x) is dependent on the wavelength region. The optical bandgap of the nanocomposite samples is decreased as the content of ZMO phase increased. The effect of alloying on the refractive index, extinction coefficient, dielectric constant, optical conductivity, and the nonlinear optical behaviors of all samples were studied in detail. The nanocomposite sample $x = 0.5$ disclosed upgraded optical parameters with the highest refractive index, optical conductivity, and PL intensity, which nominate it to be functional in various application fields.

Keywords: MFO and ZMO composite, XPS, structure, optical

PACS: 71.20.Nr, 78.55.–m, 81.07.Bc **DOI:** 10.1088/1674-1056/ac600f

1. Introduction

Multi-functional nanocomposite materials represented a newly emerging research area for the progressive development of nanotechnology.[1–3] Ferrite materials have a small bandgap therefore they easily converted the visible light energy into chemical energy to support the oxidation and reduction process.[4] Manganese ferrite ($MnFe_2O_4$, MFO) is an efficient visible light-responsive nano-photocatalyst with a narrow bandgap of 2.0 eV $\pm$ 0.5 eV.[5] Zinc manganite ($ZnMn_2O_4$, ZMO) has a spinel structure and is receiving attention as a result of its probable uses in batteries and supercapacitor fields.[6,7] The optical characteristics of different materials can be altered by changing their size, doped it with suitable materials or coupling it with other compounds.[8,9] For instance, the optical band gap of pure MFO is reduced from 2.46 eV to 2.12 eV and 2.47 eV for the hybridization of MFO/CeO_2/SnS_2 composites.[10] The optical bandgap of MFO was increased as it doped with Zn.[11] The novel microwave-based treatment with MoS_2-MFO composite revealed a rapid Cr (VI) reduction in aqueous solution.[12] The recovered MFO/$BiVO_4$ heterojunction was very active and stable for tetracycline degradation in the long-term process.[13] MFO/g-C_3N_4/TiO_2 nanocomposites under solar light revealed a very high photocatalytic degradation of Methyl Orange dye because of synergistic influence.[14] The coupling of MFO with ZnS in MFO/ZnS nanocomposite enhanced the heating efficiency for magnetic hyperthermia application.[15] The optoelectronic performance of MFO was improved as it decorated with Co_3O_4 nanorods.[16] Core double-shell MFO@rGO@TiO_2 superparamagnetic photocatalyst represented a promising material for the waste-water treatment procedure.[17] The relatively narrow bandgap of Fe- or Cr-doped ZMO together with the small dielectric properties nominated the produced materials to applied optoelectronic field.[18,19] In the present study, the influence of alloying between nano MFO and ZMO phases on the produced nanocomposite materials was examined employing Rietveld refinement procedure, x-ray photoelectron spectroscopy (XPS), Fourier-transform infrared spectroscopy (FTIR), and transmission electron microscope (TEM) techniques. Furthermore the effect of alloying on optical characteristics of the resulted nanocomposite was explored using the photoluminescence and ultra-violet (UV) diffused absorption devices.

2. Methods and materials

$(1-x)MnFe_2O_4/xZnMn_2O_4$ ($x = 0$, 0.2, 0.5, 0.8, and 1.0) samples were prepared employing co-precipitation procedure Fig. 1. The required amount from zinc acetate, manganese

†Corresponding author. E-mail: mbm1977@yahoo.com

© 2022 Chinese Physical Society and IOP Publishing Ltd

acetate and iron nitrate were dissolved in distilled water and ethylene glycol using a magnetic stirrer and heating at 90 °C (3 h). The resulted precursors were further heated at 400 °C (2 h) and the powder materials were produced. The x-ray diffraction data (XRD) were carried out using x-ray diffractometer (PANalytical with copper source). The UV diffuse reflectance data were obtained using a double-beam spectrophotometer (Shimadzu UV–VIS-2600) with attached integrating sphere assembly. The photoluminescence emission data were collected using a spectrofluorometer (Jasco FP-6500, Japan, Xenon lamb, 150 Watt) technique. FTIR spectrometer (Bruker Tensor 27) technique was used to trace the different vibration bands in different samples. The nano nature of 0.8 sample as an example was explored using a high transmission electron microscope (JEOL JEM-2100, 200 keV). Different oxidations states for different elements in the studied materials were explored by using the x-ray photoelectron spectroscopy (XPS, Thermo Scientific XPS, Model: KALPHA surface analysis) technique.

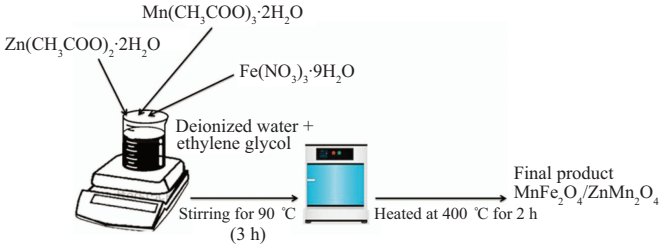


Fig. 1. Preparation schema for $MnFe_2O_4$ /$ZnMn_2O_4$ nanocomposite system.

The direct optical band gap was calculated using Tauc's and Beer–Lambert's formulas[20,21]

$$\alpha h\nu = B(h\nu - E_g)^{0.5}, \tag{1}$$

$$\alpha = \frac{2.303A}{d}, \tag{2}$$

$$\alpha = B(hc)^{n-1}\lambda\left(\frac{1}{\lambda} - \frac{1}{\lambda_g}\right)^n, \tag{3}$$

$$A(\lambda) = D\lambda\left(\frac{1}{\lambda} - \frac{1}{\lambda_g}\right)^n + D_2. \tag{4}$$

Furthermore, the extinction coefficient (k), refractive index (n), real (ε_r) and imaginary (ε_i) dielectric constants, dielectric loss ($\tan\delta$), the optical conductivities (σ_{opt}), linear optical susceptibility ($\chi^{(1)}$), the third-order nonlinear optical susceptibility (χ^3), and the nonlinear refractive (n_2) can be obtained from[21]

$$k = \frac{\lambda\alpha}{4\pi}, \tag{5}$$

$$n = \frac{1+R}{1-R} + \sqrt{\frac{4R}{(R-1)^2} - k^2}, \tag{6}$$

$$\varepsilon_r = n^2 - k^2, \tag{7}$$

$$\varepsilon_i = 2nk, \tag{8}$$

$$\tan\delta = \frac{\varepsilon_r}{\varepsilon_i}, \tag{9}$$

$$\sigma_{opt} = \frac{\alpha nC}{4\pi}, \tag{10}$$

$$\chi^{(1)} = \frac{1}{4\pi}(n^2 - 1), \tag{11}$$

$$\chi^3 = 1.7\times10^{-10}(\chi^{(1)})^4 = 1.7\times10^{-10}\left(\frac{n^2-1}{4\pi}\right)^4, \tag{12}$$

$$n_2 = \frac{12\pi}{n}\chi^{(3)}, \tag{13}$$

where A, d, E_g, B, $h\nu$, λ_g, h, c, ($D_1 = [B(hc)^{n-1}d/2.303]$, D_2), λ, and R are the absorbance, thickness, optical band gap, constant, incident photon energy, the wavelength related to the optical gap, Planck's constant, light velocity, constants represent reflection, wavelength, and reflectance, respectively.

3. Results and discussion

3.1. Crystal structure and phase analysis

The high quality x-ray diffraction patterns measured for $(1-x)MnFe_2O_4/xZnMn_2O_4$ ($x = 0$, 0.2, 0.5, 0.8, and 1.0) are given in Fig. 2(a). Structural analysis applying Rietveld method implanted in the program MAUD[22,23] manifested the presence of two phases for the composites $x = 0.2$ and 0.5: $ZnMn_2O_4$ (ZMO) with tetragonal spinel structure (S.G. I 4_1/a m d), and $MnFe_2O_4$ (MFO) with cubic spinel structure (Fd-$3m$), while only singlephase ZMO is found for the sample $x = 0.8$. Figure 2(b) illustrates the resulting fitting for diffraction pattern for $x = 0.5$ and the resulting refined parameters are given in Table 1.

Table 1. The cell parameters (in unit Å), average crystallite size (in unit nm), and the phase percentages of the phases developed in the heterostructure nanocomposite $(1-x)MnFe_2O_4/xZnMn_2O_4$ ($x = 0$, 0.2, 0.5, 0.8, 1.0) for different values of x.

x	Size (nm)	$ZnMn_2O_4$			$MnFe_2O_4$		
		a (Å)	c (Å)	%	a (Å)	%	Size (nm)
0	–	–	–	–	8.3910	100	19.5
0.2	9.8	5.7667	9.0615	24.4	8.4086	75.6	19.7
0.5	11.7	5.8330	8.7841	55.3	8.2650(5)	44.7	14.7
0.8	9.3	5.7753	9.0087	100	–	–	–
1.0	21.6	5.7345(7)	9.1937(11)	100	–	–	–

The phase percentages of MFO and ZMO phases are different from the nominated values during preparation, which requires the incorporation of the cation of one phase into the lattice of the other phase; this confirmed the result concluded from IR analysis next. Such cation permutation among the octahedral and tetrahedral sites changes the cell parameters of the phases, (see Table 1). The cell parameter (a) of MFO altered irregularly, it slightly rose for $x = 0.2$ and reduced for $x = 0.5$. For ZMO phase, the cell parameter (c) reduced while the parameter (a) slightly rose with the alloying parameter (x). This could be correlated with cation permutation as follows: the ZMO octahedra, figure 2(c) has a base in the ab-plane direction with four O-ions of equal bond length with the cation at the center ($\sim$ 1.97 Å), and two apex O-atoms along the c axis with bond length = 2.28 Å. Insertion of Fe^{3+}ions of electronegativity (1.83) higher than that of Mn^{3+} ions (1.55) results in shortening the longer bond length of the octahedra along the c axis, *i.e.*, compressing the octahedra along the c axis. Consequently, the cell parameter (a) rose slightly. The crystallite size is hardly altered upon varied alloying parameter (x) as displayed in Table 1. The TEM image for sample with $x = 0.8$ is displayed in Fig. 2(d). It could be noticed that the particle size is in the nano range around 20 nm.

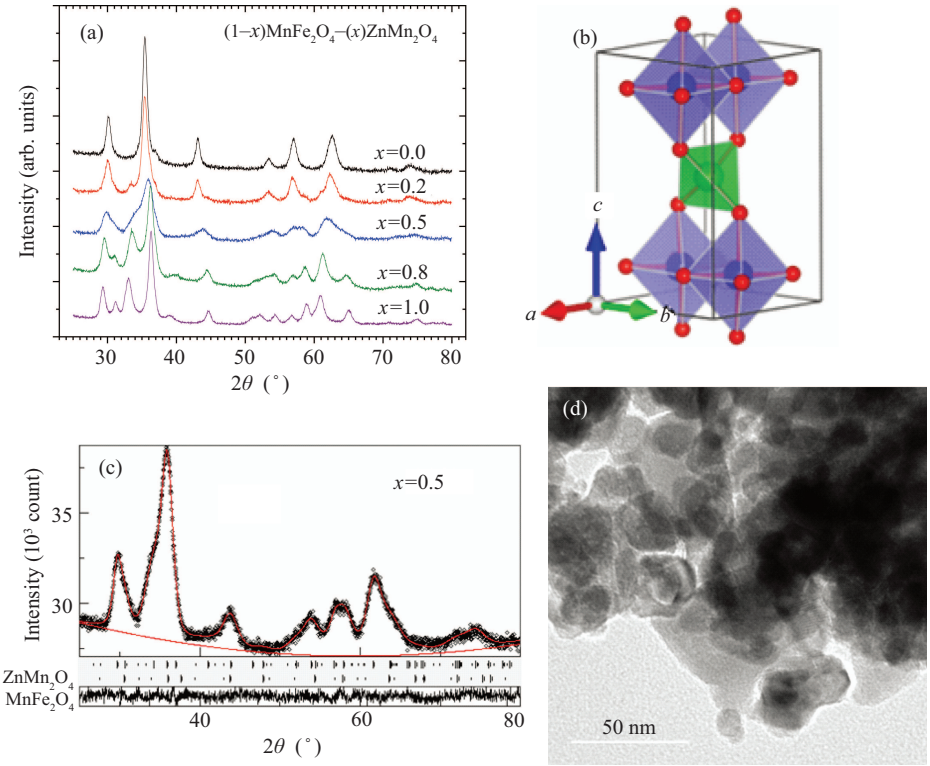


Fig. 2. (a) X-ray diffraction patterns for $(1-x)$ $MnFe_2O_4$ + $xZnMn_2O_4$ nanocomposite samples, (b) Rietveld refinement pattern fitting for sample with $x = 0.5$, (c) crystal structure of $ZnMn_2O_4$ phase, and (d) TEM image for sample with $x = 0.8$.

Infrared absorption (vibrational) spectroscopy is bond specific and commonly employed to characterize transition metal–oxygen species. For this purpose, FTIR spectra for the present system $(1-x)MnFe_2O_4/xZnMn_2O_4$ ($x = 0$, 0.2, 0.5, 0.8, and 1.0) have been measured, (see Fig. 3). The spectrum of the pure sample MFO ($x = 0.0$), has two vibrational bands observed at 552.1 cm^{-1} and 628.3 cm^{-1} which could be assigned to stretching vibrations of metal $\leftrightarrow$ O at octahedral and tetrahedral sites, respectively.[24,25] For $x = 0.2$ sample, MFO phase is the dominant, (see Table 1), so only MFO vibrational bands appeared at 554.2 cm^{-1} and 636.6 cm^{-1} for octahedral and tetrahedral vibrational bands, respectively; no characteristic bands for ZMO are observed in the spectrum. One can notice in Fig. 3 that both bands become flat and shifted to higher wavenumbers compared with $x = 0.0$, indicating that some Zn ions have been incorporated into the MFO lattice in both octahedral and tetrahedral sites. The IR spectrum of pure ZMO ($x = 1.0$) has two vibrational bands located at 506 cm^{-1} and 619 cm^{-1} which are characteristic of tetragonal spinel structure and belong to metal $\leftrightarrow$ O vibrations at octahedral and tetrahedral sites, respectively.[26,27] For the sample $x = 0.8$, only these two bands of ZMO phase appeared and no bands for MFO phase were observed. Furthermore, as indicated in Fig. 3, both vibrational bands are shifted (relative to $x = 1.0$) to lower wavenumbers, 481 cm^{-1} and 608 cm^{-1} implying that some Fe ions are incorporated into the ZMO phase in both octahedral and tetrahedral sites. For sample $x = 0.5$, both phases ZMO and MFO are formed with nearly equal percentages, so the vibrational bands of the two phases overlap yielding very flat bands as shown in Fig. 3. One can conclude that for

the nanocomposite samples, all cations have been permuted among the octahedral and tetrahedral sites of both ZMO and MFO phases. This is confirmed by the IR spectrum of the sample $x = 0.5$ where the vibrational bands become flat due to the occupation of the sites by different cations (Zn, Mn, Fe).

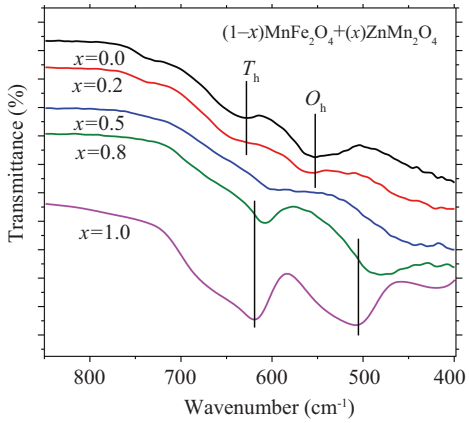


Fig. 3. FTIR spectra for $(1-x)$ $MnFe_2O_4$ + $xZnMn_2O_4$ nanocomposite samples.

3.2. XPS investigations

For further investigating the cation permutation among the two phases MFO and ZMO, the elements constituting the samples and their oxidation states are examined by measuring the XPS spectra of the sample $x = 0.5$. The XPS Gaussian fitting analyses were performed and illustrated in Fig. 4. The fitting of the Zn 2p narrow scan, (see Fig. 4(a)), disclosed two peaks at binding energies 1021.3 eV and 1044.3 eV which could be assigned to Zn^{2+} $2p_{3/2}$ and $2p_{1/2}$ energy levels. The energy difference of 23 eV coincides very well with that in literature.[28] Figure 4(b) displays the high-resolution spectrum of Fe 2p orbitals. The spectrum comprises a peak at 710.8 eV representing the binding energy of Fe^{3+} $2p_{3/2}$ level, which could be decomposed into two subpeaks at 710.35 eV and 712.7 eV assigned to Fe^{3+} at octahedral and tetrahedral sites respectively.[29] Furthermore, two satellite peaks appear at 716.3 eV and 719.5 eV to confirm the presence of Fe^{3+} cations only.[30] The highresolution XPS of Mn 2p could be fitted into four contributions, (see Fig. 4(c): two at the binding energies of 641.1 eV and 642.1 eV represent the energy level Mn 2p3/2 and are assigned to the Mn^{2+} and Mn^{3+}, respectively.[31] The other two at 652.9 eV and 653.8 eV were assigned to Mn $2p_{1/2}$ energy level. From the ratio of peak areas, the atomic ratio of Mn^{2+} to Mn^{3+} could be calculated to be 0.46 which is consistent with the phase percentage of MFO to ZMO, Table 1, where Mn^{2+} residing at MFO while Mn^{3+} residing at ZMO. Figure 4(d) depicts the O 1s narrowspectrum fitting which comprises three peaks at 529.7, 531.4, and 532.1 eV. The first is assigned to O^{2-}–metal bonding, the second is assigned to various reasons like surface OH, chemisorbed oxygen, oxygen ions in low coordination, and oxygen-containing surface contamination.[32,33] The third is attributed to surface bond water.[34]

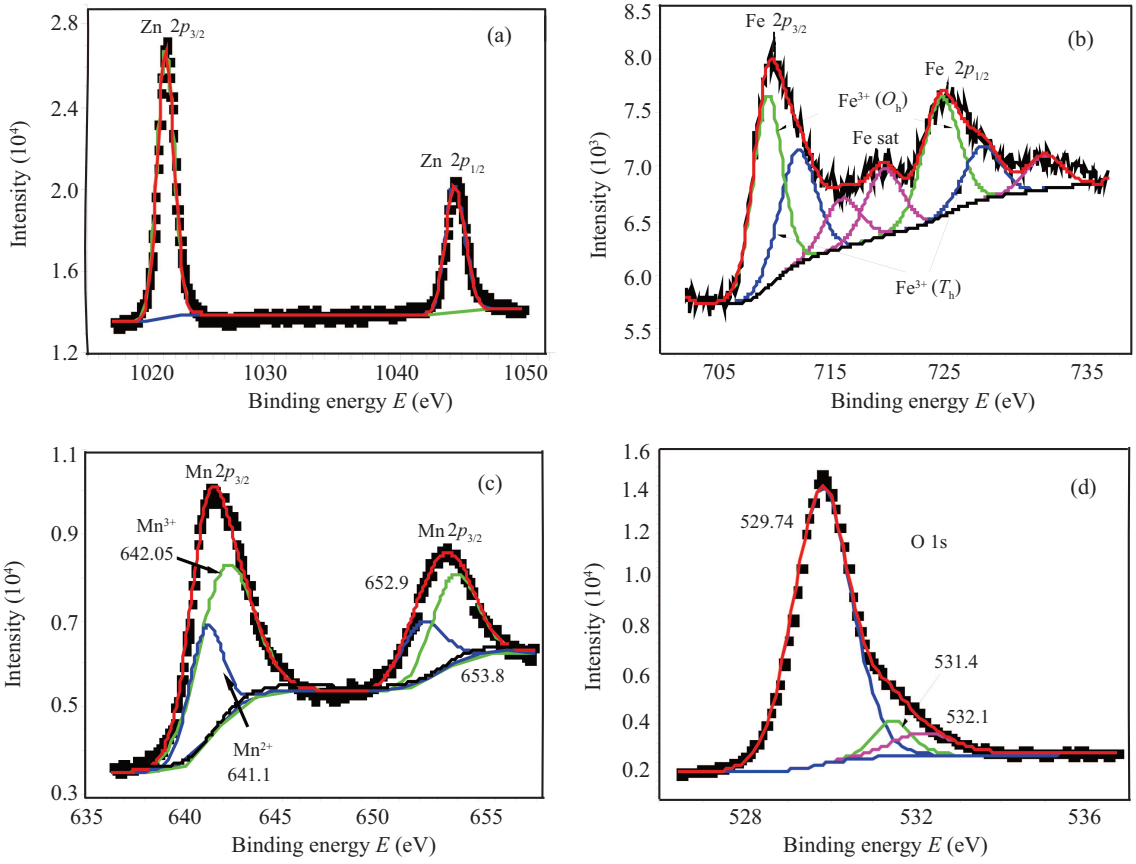


Fig. 4. XPS fitting for (a) Zn, (b) Fe, (c) Mn, and (d) O peaks for $0.5MnFe_2O_4$ + $0.5ZnMn_2O_4$ nanocomposite samples.

3.3. Optical characterization

The variation of the diffused absorbance data with the wavelength for $(1-x)ZnMn_2O_4/(x)MnFe_2O_4$ nanocomposite samples are displayed in Fig. 5.

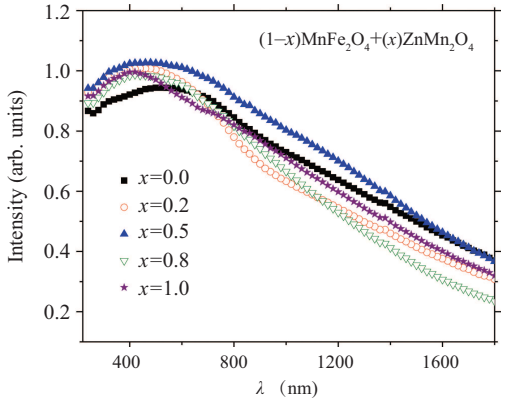


Fig. 5. The wavelength dependence of the diffused absorbance for $(1-x)$ $MnFe_2O_4 + xZnMn_2O_4$ nanocomposite samples.

As noticed from the graph the absorbance of ZMO ions is higher than the absorbance of MFO at a low wavelength range and the situation is reversed at the higher wavelength range. The absorbance of the nanocomposite samples is varied depended on the composition of the samples and the measured wavelength range. The sample with $x = 0.5$ exhibited the highest absorbance among all samples. The change in the absorbance may be due to the variation of the charge trapping effect on the sample surface as a result of the shallow energy level impurities.[35] The direct optical band gap energy (E_g) of the nanocomposite samples can be extracted from the linear intercept of $(ahv)^2$ as a function of hv graph as established in Fig. 6. The obtained optical band gaps of MFO and ZMO samples are 2.68 eV and 2.13 eV, respectively. The obtained optical band gaps are in agreement with that obtained by other research groups, for example, the optical band gap of MFO formed by a facile hydrothermal route is 2.46 eV while the E_g of MFO prepared by reverse-micelle synthesis strategy is 2.65 eV.[10,36] The E_g value for ZMO sample prepared by the solgel method is 1.28 eV.[37] Furthermore, the optical bandgap of $(1-x)$MFO/xZMO ($x = 0.2$, 0.5, 0.8) nanocomposite samples are 2.55, 2.54, and 2.63 eV. As noticed from the figure the optical bandgap of the nanocomposite samples is decreased as the amount of ZMO phase (less optical bandgap than MFO) increased in the samples, see Table 1. The band gap of MFO is 2.65 eV and that of ZMO is 2.13 eV, so most probable the band gap of intermediate composites will be in between, so it decreases by adding ZMO. The raising of the optical bandgap in the nanocomposite sample with $x = 0.8$ instead of decreasing is due to the increasing of ZMO amount may be due to the formation of single-phase of ZMO, see Table 1. This increase in the optical band gap may be due to the introduction of Fe ions inside the ZMO matrix (x-ray part) which may alter the optical band gap characteristics of the host matrix. The refractive index (n) reflected the interaction between the photons and electrons in the materials.

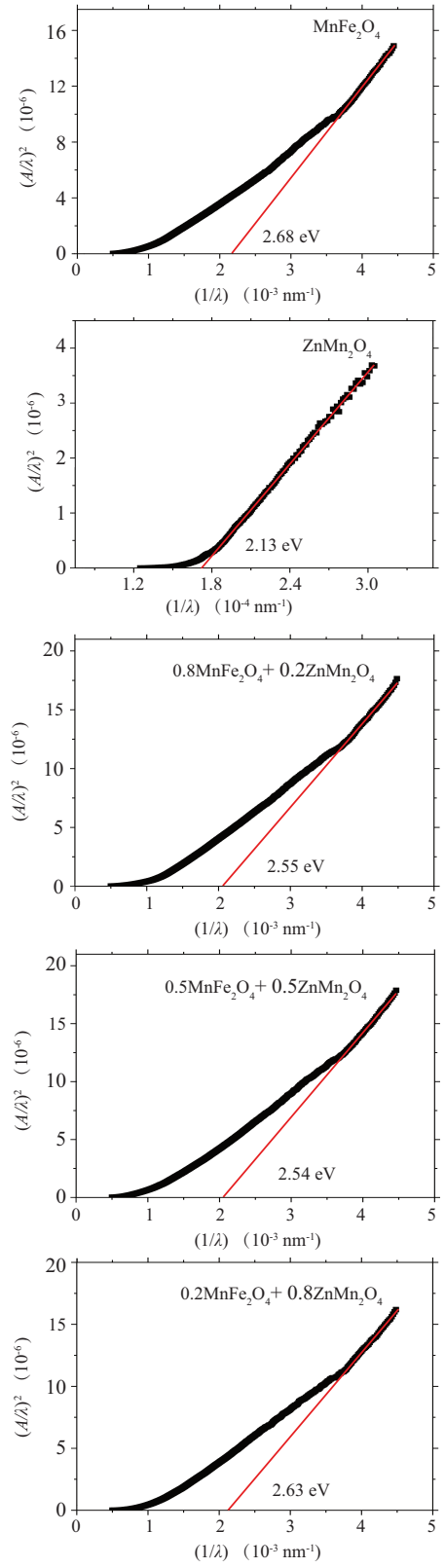


Fig. 6. The relation between $(A/\lambda)^2$ *versus* photon energy ($h\nu$) for $(1-x)MnFe_2O_4 + xZnMn_2O_4$ nanocomposite samples.

Figure 7(a) shows the changing of the refractive index (n) with wavelength for all samples. All samples exhibited a nor-

mal dispersion. The n value of ZMO sample is higher than the n value of MFO sample. At the low wavelength range, MFO sample has the lowest n value while at a higher wavelength range, the sample with $x = 0.8$ has the lowest n value. In the visible range, the n values of the nanocomposite samples are larger than the n value of MFO. In addition, the n values of the samples with $x = 0.2$ and 0.5 are larger than ZMO sample in the visible range. The enhancement of the refractive index may be due to the change in the electronic structure of the MFO and ZMO materials upon alloying. Furthermore, the improvement of the n values is inferred from the improvement of the sensitivity of nanocomposite samples with $x = 0.2$ and 0.5 to the daylight.

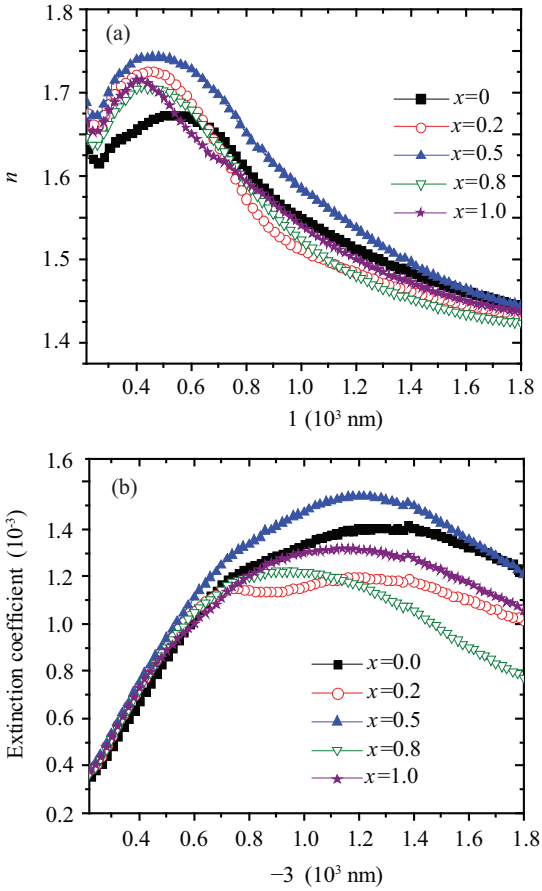


Fig. 7. The wavelength dependence of (a) refractive index (n) and (b) extinction coefficient (k) for $(1-x)$ $MnFe_2O_4$ + $xZnMn_2O_4$ nanocomposite samples.

Figure 7(b) displays the variation of the extinction coefficient (k) against wavelength for all nanocomposite samples. As noticed from the figure the behavior of k values in all samples are similar where the k value increased with increasing the wavelength until it reached its highest value then it decreased again. Sample with $x = 0.5$ in the $(1-x)$MFO/xZMO nanocomposite system has the highest k value while the sample with $x = 0.8$ has the lowest value.

The wavelength-dependent of the dielectric constant (real and imaginary) and dielectric loss for $(1-x)$MFO/xZMO nanocomposite samples is represented in Fig. 8. As revealed from Fig. 8(a), the real part of the dielectric constant (ε_r) has the highest value at a low wavelength range for all samples them it decreased with increasing the wavelength similar to the refractive index behavior. The low dielectric constants at a higher wavelength range restrain the electromagnetic energy propagation that contributes to the conductivity. Furthermore, the free carriers are activated and shared the conduction. On the other hand, the dielectric constant (ε_i) and dielectric loss ($\tan\delta$) increased with increasing the wavelength until it reaches the maximum value then it decreased with increasing the wavelength similar to the k value behavior. In addition, nanocomposite with $x = 0.5$ has the highest ε_r, ε_i, and $\tan\delta$ values as compared with other samples.

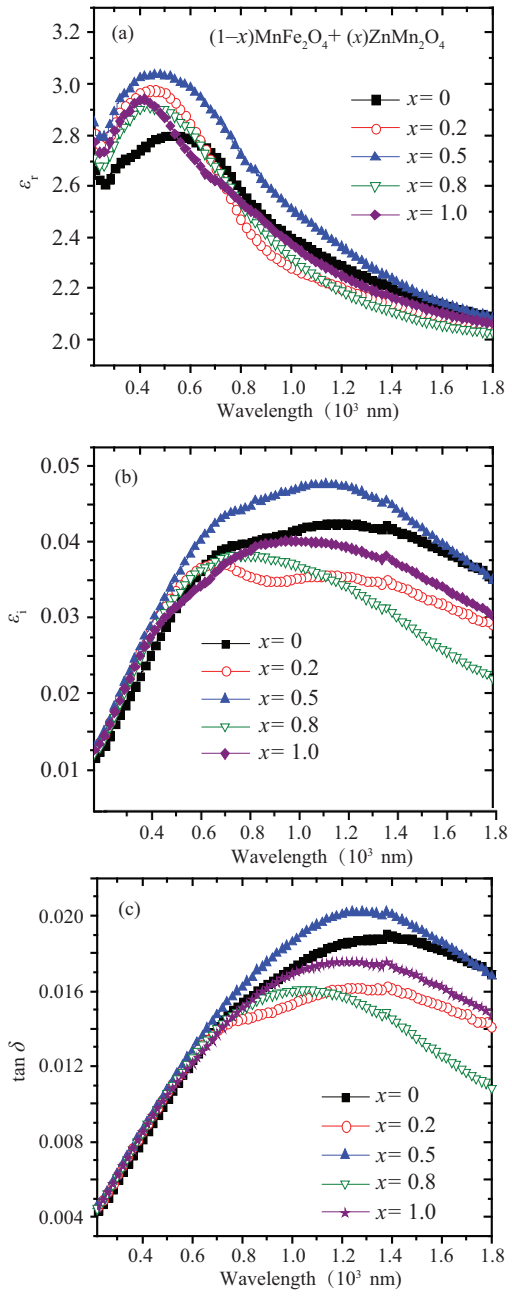


Fig. 8. The wavelength dependence of the (a) real part (ε_r), (b) imaginary part (ε_i) of dielectric constant and (c) $\tan\delta$ for $(1-x)$ $MnFe_2O_4$ + $xZnMn_2O_4$ nanocomposite samples.

The variation of the optical conductivity (σ_{opt}) for all nanocomposite samples with photon energy is revealed in Fig. 9. The σ_{opt} values in all samples were increased as the photon energy increased. The σ_{opt} value for the nanocomposite sample with $x = 0.5$ has the highest value among the other samples. The changes in $\chi^{(1)}$, n_2, and $\chi^{(3)}$ values with the wavelength for all $(1-x)ZnMn_2O_4/(x)MnFe_2O_4$ nanocomposite samples are represented in Fig. 10. All the three parameters exhibited a similar behavior, where $\chi^{(1)}$, n_2, and $\chi^{(3)}$ values are decreased with increase the wavelength. All samples have $\chi^{(1)}$, n_2, and $\chi^{(3)}$ values larger than MFO sample. Sample with $x = 0.5$ has the highest $\chi^{(1)}$, n_2, and $\chi^{(3)}$ values as compared with other samples. This result indicates the nanocomposite sample with $x = 0.5$ has a good nonlinear optical behavior in all wavelength range.

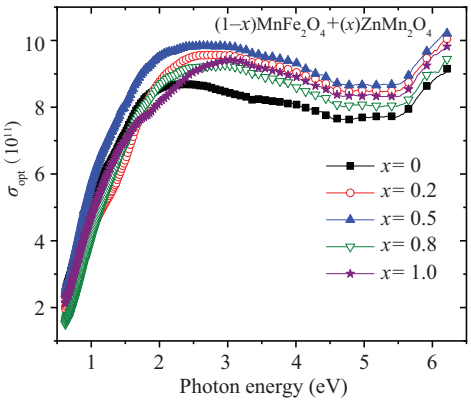


Fig. 9. The variation of the optical conductivity for $(1-x)MnFe_2O_4$ + $xZnMn_2O_4$ nanocomposite samples with photon energy.

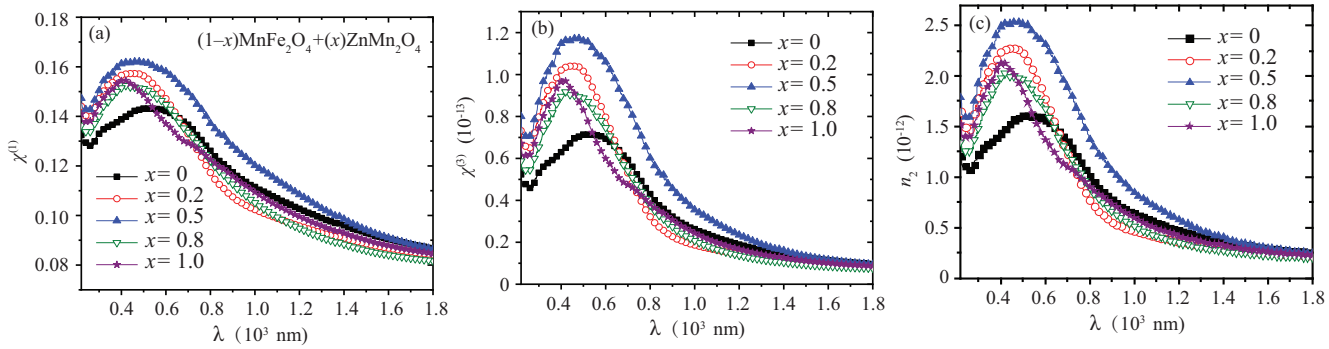


Fig. 10. The Relation between (a) χ^1, (b) χ^3, (c) n^2, and wavelength for $(1-x)MnFe_2O_4$ + $xZnMn_2O_4$ nanocomposite samples.

3.4. Photoluminescence (PL) emissions

Figure 11 reveals the photoluminescence (PL) data for $(1-x)$MFO/xZMO samples at room temperature by using 350-nm excitation wavelength. The PL intensity of the ZMO sample is higher than the PL intensity of the MFO sample. Furthermore, the PL intensities of the nanocomposite samples are between the PL intensities of MFO and ZMO samples. Sample with $x = 0.2$ has the lowest intensity while the sample with $x = 0.5$ exhibited the highest PL intensity. Similar results were obtained where the PL intensity reduced upon doping or forming composites: for ZnS upon coupling with MFO,[39] for intermediate nanocomposites of MnS@ZnS system,[38] and for ZMO upon doping with Fe[18] or Cr.[19] In contrast Patade *et al*. found that as MFO doped with Zn, the PL intensity increased.[11] The variation of the PL intensity may result from changing of the recombination rate between the photo-induced electrons (e) and holes (h^+) pairs created in the different samples which are depended on the trap levels produced in the bandgap upon alloying.[40,41] The reduction in the PL intensity of the nanocomposite samples may nominate them to be applied in the photocatalytic area. By using Gaussian fitting the PL of each sample can be divided into sub emission peaks. Moreover, the possible transition of electrons between different levels is also provided in Fig. 12. As noticed from the graph and Table 2 that the PL spectra of all samples except nanocomposite samples with $x = 0.5$ and 0.8 are formed from two violets, blue and green colors. Samples with $x = 0.5$ and $x = 0.8$ emitted (two violets, blue) and (violet, blue, green) colors, respectively. The MFO formed by the co-precipitation procedure emitted a green color.[11] The disorder in the lattice or interstitial oxygen defects formed in the samples formed a green emission.[42]

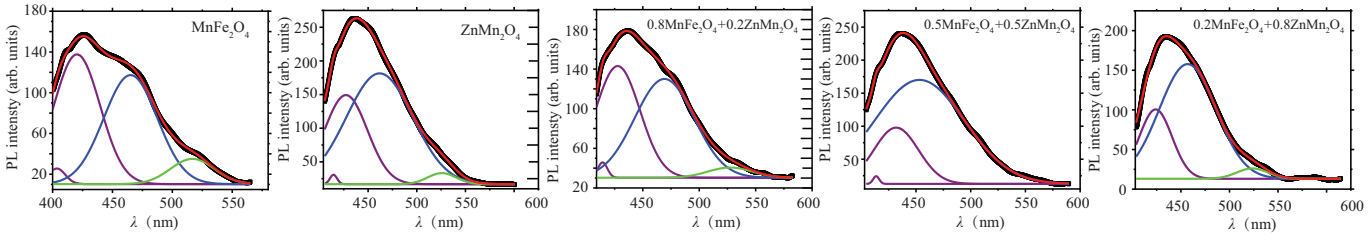


Fig. 11. The Gaussian fitting for photoluminescence measurements under 350 nm for $(1-x)MnFe_2O_4$ + $xZnMn_2O_4$ nanocomposite samples.

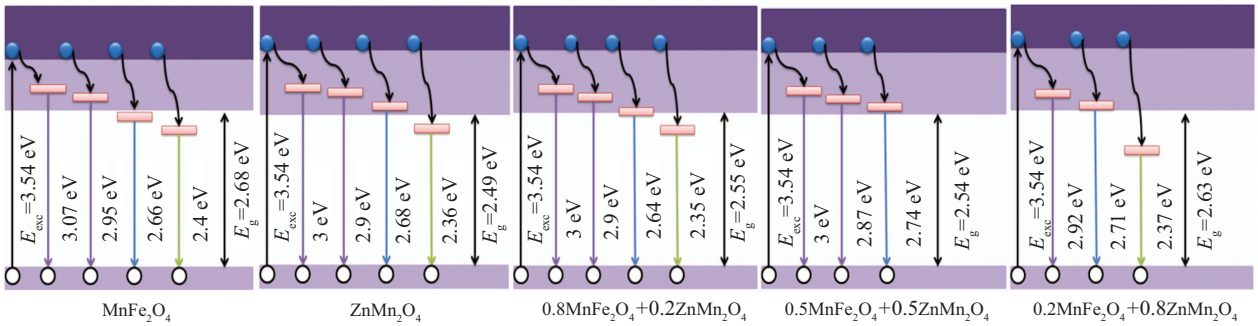


Fig. 12. Schematic of various possible transitions for $(1-x)MnFe_2O_4 + xZnMn_2O_4$ nanocomposite samples.

Table 2. PL peak positions for the nanocomposite $(1-x)$ $MnFe_2O_4 + xZnMn_2O_4$ for different values of x.

Sample	PL emission peaks in nm at 350-nm excitation wavelength
$MnFe_2O_4$	(404, 420) (V), 465 (B), 517 (G)
$0.8MnFe_2O_4 + 0.2ZnMn_2O_4$	(414, 428) (V), 469 (B), 527 (G)
$0.5MnFe_2O_4 + 0.5ZnMn_2O_4$	(414, 432) (V), 453 (B)
$0.2MnFe_2O_4 + 0.8ZnMn_2O_4$	424 (V), 457 (B), 524 (G)
$ZnMn_2O_4$	(414, 427) (V), 462 (B), 526 (G)

4. Conclusions

Nanocomposites $(1-x)MnFe_2O_4/xZnMn_2O_4$ with $x = 0.2$ and 0.5 have $ZnMn_2O_4$ (ZMO) with tetragonal spinel structure and $MnFe_2O_4$ (MFO) with cubic spinel structure, while only single-phase ZMO is found for the sample with $x = 0.8$. The cell parameter (a) of MFO changed irregularly, for ZMO phase, the cell parameter (c) reduced while (a) slightly increased with the alloying parameter (x). The IR analysis and the variation in the lattice parameters confirmed permutation all cation among the octahedral and tetrahedral sites of the two phases in the intermediate samples. The XPS analysis revealed that Mn^{2+} residing at MFO while Mn^{3+} residing at ZMO. Sample with $x = 0.5$ exhibited the highest optical absorbance among all samples. The obtained optical band gaps of MFO and ZMO samples are 2.68 eV and 2.13 eV, respectively; and of nanocomposite samples, $x = 0.2$, 0.5, and 0.8 are 2.55, 2.54, and 2.63 eV respectively. Relative to the pure sample ZMO and MFO, the variation in refractive index of the nanocomposite samples with (x) is dependent on the wavelength region, except for $x = 0.5$ sample which has the highest (n) value for the whole λ range. Also, sample with $x = 0.5$ disclosed the highest ε_r, ε_i, $\tan\delta$, σ_{opt}, and PL intensity values and a good nonlinear optical behavior as compared with other samples. The PL spectra of all samples except $x = 0.5$ and 0.8 are formed from two violets, blue and green colors. Sample with $x = 0.5$ and 0.8 emitted (two violets, blue) and (violet, blue, green) colors, respectively.

Acknowledgment

The authors acknowledge Taif University Research Supporting Project number (TURSP-2020/66), Taif University, Taif, Saudi Arabia.

References

[1] Heiba Z K, Mohamed M B, El-naggar A M and Altowairqi Y 2021 *Appl. Phys. A* **127** 1
[2] Heiba Z K, Deyab M A, El-naggar A M and Mohamed M B 2021 *Ceram. Int.* **47** 7475
[3] Farag N M, Deyab M A, El-naggar A M, Aldhafiri A M, Mohamed M B and Heiba Z K 2021 *J. Mater. Res. Technol.* **10** 1415
[4] Meena S, Anantharaju K S, Vidya Y S, Renuka L, Uma B, Sharma S C, Prasad B D and More S S 2021 *Ceram. Int.* **47** 14760
[5] Li X, Hou Y, Zhao Q and Wang L 2011 *J. Colloid Interface Sci.* **358** 102
[6] Heiba Z K, Ghannam M M, Sanad M M S, Albassam A A and Mohamed M B 2020 *J. Mater. Sci.: Mater. Electron.* **31** 8946
[7] Ghannam M M, Heiba Z K, Sanad M M S and Mohamed M B 2020 *Appl. Phys. A* **126** 1
[8] Heiba Z K, Albassam A A and Mohamed M B 2020 *Appl. Phys. A* **126** 1)
[9] Heiba Z K and Mohamed M B 2020 *J. Inorg. Organomet. Polym. Mater.* **30** 879
[10] Zhao W, Wei Z, Zhang X, Ding M, Huang S and Yang S 2020 *Appl. Catal. A: Gen.* **593** 117443
[11] Patade S R, Andhare D D, Kharat P B, Humbe A V and Jadhav K M 2020 *Chem. Phys. Lett.* **745** 137240
[12] Pang Y, Kong L, Chen D and Yuvaraja G 2019 *Appl. Surf. Sci.* **471** 408
[13] Cam N T D, Pham H D, Pham T D, et al. 2021 *Ceram. Int.* **47** 1686
[14] Vignesh K, Suganthi A, Min B K and Kang M 2014 *J. Mol. Catal. Chem.* **395** 373
[15] Mondal D K, Borgohain C, Paul N and Borah J P 2019 *Physica B: Condens. Matter* **567** 122
[16] Chinnathambi A, Nasif O, Alharbi S A and Khan S S 2021 *Mater. Sci. Semicond. Process.* **134** 105992
[17] Abdel-Wahed M S, El-Kalliny A S, Badawy M I, Attia M S and Gad-Allah T A 2020 *Chem. Eng. Sci.* **382** 122936
[18] Heiba Z K, Mohamed M B, Ghannam M M, El-naggar A M and Altowairqi Y 2021 *J. Mater. Sci.: Mater. Electron.* **32** 19529
[19] Heiba Z K, Mohamed M B, Ghannam M M and Ahmed S I 2021 *Appl. Phys. A* **127** 1
[20] Tauc J, Grigorovici R and Vancu A 1966 *Phys. Status Solidi* **15** 627
[21] Heiba Z K, Mohamed M B, Badawi A and Alhazime A A 2021 *Chem. Phys. Lett.* **770** 138460
[22] Rodríguez-Carvajal J 1993 *Physics B (Amsterdam, Neth.)* **192** 55
[23] Lutterotti L 2010 *Phys. Res. B* **268** 334

[24] El-naggar A M, Mohamed M B, Aldhafiri A M and Heiba Z K 2020 *J. Mater. Res. Technol.* **9** 16435

[25] Heiba Z K and Mohamed M B 2018 *Appl. Phys. A* **124** 1

[26] Gherbi R, Bessekhouad Y and Trar M 2016 *J. Alloys Compd.* **655** 188

[27] Heiba Z K, Shaltout A A, Ahmed S I, Alzahrani E, Wahba H H, Deyab M A and Mohamed M B 2021 *Appl. Phys. A* **127** 1

[28] Fan B B, Hu A P, Chen X H, Zhang S Y, *et al.* 2016 *Electrochim. Acta* **213** 37

[29] Yin L, Adler I, Tsang T, Matienzo L and Grim S 1974 *Chem. Phys. Lett.* **24** 81

[30] Hong D, Yamada Y, Nagatomi T, Takai Y and Fukuzumi S 2012 *J. Am. Chem. Soc.* **134** 19572

[31] Xue P, Jiang S, Li W, Shi K, Ma L and Li P 2021 *Bioprocess. Biosyst. Eng.* **44** 1119

[32] Zhang C, Xie A, Zhang W, Chang J, Liu C, Gu L, Duo X, Pan F and Luo S 2021 *J. Energy Storage* **34** 102181

[33] Wang D W, Wang Q H and Wang T M 2011 *Inorg. Chem.* **50** 6482

[34] Koninck M D, Poirier S C and Marsan B 2006 *J. Electrochem. Soc.* **153** 2103

[35] Tao X, Shi W, Zeng B, Zhao Y, Ta N, Wang S, Adenle A A, Li R and Li C 2020 *ACS Catal.* **10** 5941

[36] Baig M M, Zulfiqar S, Yousuf M A, Touqeer M, Ullah S, Agboola P O, Warsi M F and Shakir I 2020 *Ceram. Int.* **46** 23208

[37] Gherbi R, Bessekhouad Y and Trari M 2016 *J. Phys. Chem. Solids* **89** 69

[38] Heiba Z K, Mohamed M B, Ahmed S I, El-naggar A M and Albassam A A 2020 *J. Mater. Sci.: Mater. Electron.* **31** 14746

[39] Mondal D K, Borgohain C, Paul N and Borah J P 2019 *Physica B: Condens. Matter* **567** 122

[40] Singha D K and Mahataa P 2017 *Dalton Trans.* **46** 11344

[41] Heiba Z K, Mohamed M B and Imam N G 2017 *J. Supercond. Nov. Magn.* **30** 3123

[42] Manikandan A, Vijaya J J, Kennedy L J and Bououdina M 2013 *J. Mol. Struct.* **332** 1035